University of Nevada

Reno

In Search of Target Excitation in Low Energy Ion-Atom Collisions

A thesis submitted in partial fulfillment

of the requirement for the degree of

Master of Science in Physics

by

Haci Mustafa Cakmak

Dr. Rami M. Ali, Thesis Advisor

November 1996, Reno

The thesis of Haci Mustafa Cakmak is approved :

Rami M. Ali

Thesis Advisor

Ronald A Pfahnl

Department Chairman

Dean, Graduate School

University of Nevada

Reno

November 1996

CONTENTS

Acknowledgments

I would like to express my immense gratitude to Dr. Rami M. Ali, my advisor, for giving me the opportunity to work with him. I also would like to thank my committee members, Prof. Reinhard B 3ruch and Prof. Joseph I. Cline for helpful discussions and their review of this thesis.

I would like to express my sincere appreciation to Dr. Hocine Merabet, Ahmad Hasan and Timur Osipov for their help at different stages of my work. I also would like to thank Prof. Ronald A. Phaneuf, Riad Rejoub and Victoria Golvokina for their cooperation. Special thanks are extended to the Physics Department electronics and machine shops Staff, Mr. Bill Brinsmead, Mr. Wade Cline, Mr. Dennis Meredith and Mr. Walt Weaver.

Special thanks are extended to my friends Faruk Taban, Raif Kurtaran, Nizamettin Gul, Unal Yildirim, Yunus Cerci and others.

Finally, my thanks go to my wife and my daughters, my parents and my brothers and sisters, for their continuous encouragement and support.

List of Figures

List of Tables

Chapter 1

Introduction

The study of the different processes involving ion-atom collisions attracted a great deal of interest during the last few decades. Indeed, the development of new ion sources such as the electron cyclotron resonance (ECR) and electron-beam ion sources (EBIS) has opened new perspectives in this area. In particular, the ECR sources provide intense beams of highly charged ions to be used in collision experiments at different energies. The analyses of the data obtained from such collisions help us better understand the atomic processes occurring in fusion reactor plasmas, X-ray lasers, and astrophysical settings.

When an ion A^{q+} collides with a multi-electron target B, several processes may occur such as :

$A^{q+} + B$	$\rightarrow$	$A^{q+} + B^*$	Target excitation
$A^{q+} + B$	$\rightarrow$	$A^{q+} + B^{r+} + re^-$	Target ionization
$A^{q+} + B$	$\rightarrow$	$A^{(q-r)+*} + B^{r+}$	Charge transfer + projectile excitation
$A^{q+} + B$	$\rightarrow$	$A^{(q-r)+*} + B^{r+*}$	Charge transfer + target excitation

The relative importance of these processes depends not only on the projectile charge state and number of target and projectile electrons, but also on the projectile

velocity v. In particular, three velocity domains are defined when comparing v with the classical velocities of the active electrons v_i:

- the domain of high collision velocities : $v > \text{Max}\ \{v_i\}$
- the domain of intermediate collision velocities : $v \approx \{v_i\}$
- the domain of low collision velocities : $v < \text{Max}\{v_i\}$

Ionization and excitation are the dominant phenomena at high collision velocities, while charge transfer dominates at low velocities.

In general, the processes cited above leave the projectile, the target or both in excited states. After the collision, these states decay either by Auger electron emission or by photon emission. Radiative and nonradiative decay processes allow the experimental investigation of the mechanisms involved in ion-atom collisions by means of photon spectroscopy and Auger electron spectroscopy [1]. Other spectroscopic techniques such as translational energy gain/loss [1] and recoil ion momentum spectroscopy [2] have also been used to investigate such collisions.

This thesis describes the installation of a new beamline at the multi-charged ion facility in the Department of Physics at the University of Nevada, Reno. This beamline will be used to investigate multi-electron processes in slow collisions of highly charged ions with many-electron targets by means of time-of-flight (TOF) spectroscopy, recoil ion momentum spectroscopy, Auger electron spectroscopy and photon spectroscopy.

In addition to the present status of the experimental setup, the results of some preliminary experiments, involving the detection of vacuum ultraviolet (VUV) photons, in search of signatures for the process of transfer-target excitation will be discussed.

Chapter 2

Experimental Setup

2.1. The ECR Ion Source

The source of the projectile ions is a CAPRICE ECR ion source [3,4] installed in the Department of Physics at the University of Nevada, Reno. A schematic of the multi-charged ion research facility [5] is shown in Fig. 1. In the ECR ion source, electrons are confined by a magnetic bottle formed by two parallel solenoids and a hexapole permanent magnet. The cyclotron motion of the electrons in the magnetic field is resonantly excited by a microwave-frequency electromagnetic field. A low-pressure gas or metal vapor is admitted into the plasma chamber and becomes highly ionized by successive collisions with the hot electrons. Ions are pulled out of the plasma chamber, which is held at a positive potential, with a grounded Pierce extraction electrode. The ion-beam transport and analysis system delivers mass-to-charge (q/m) analyzed ion beams to the experimental stations while preserving the charge integrity.

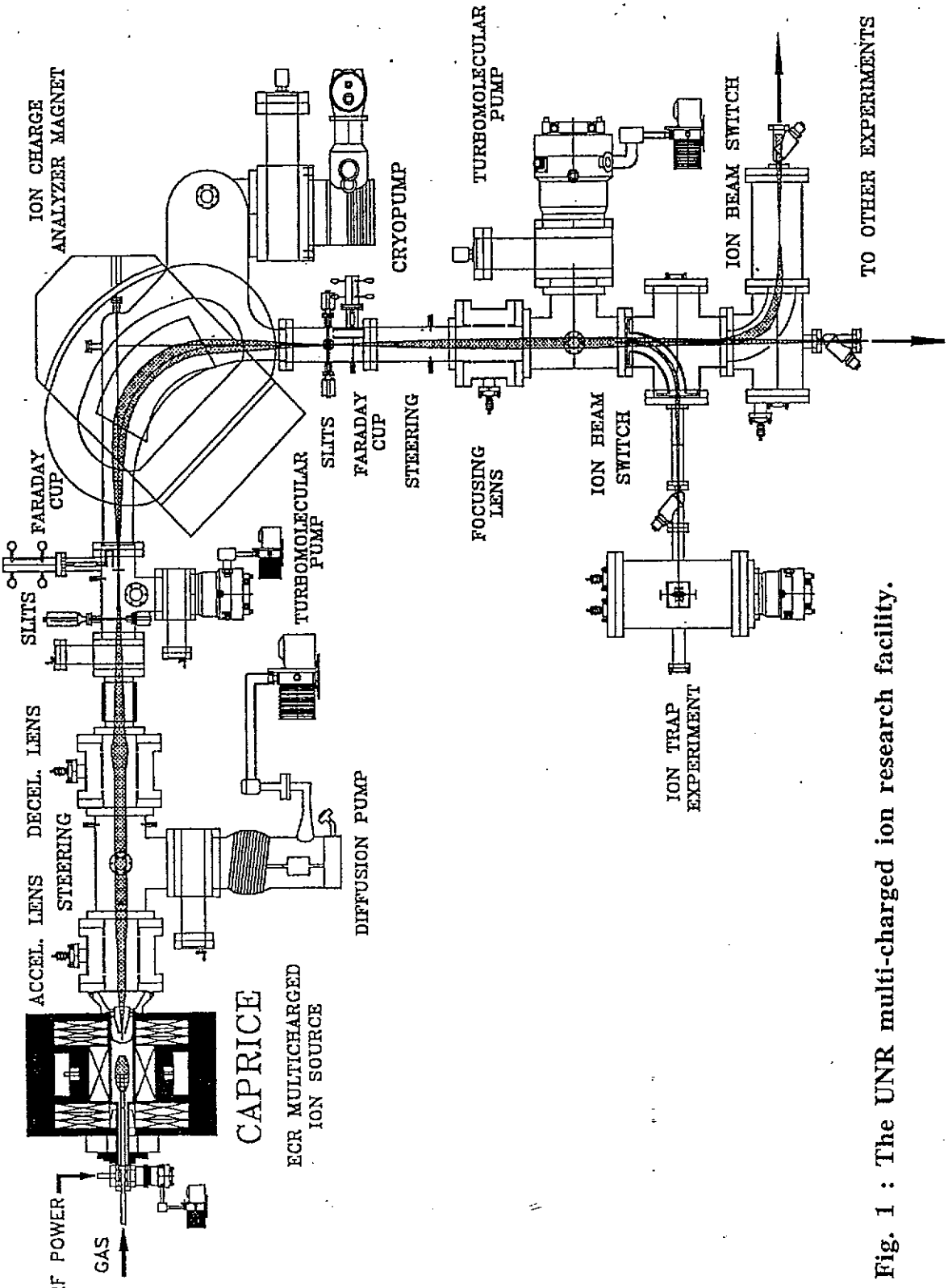

Fig. 1 : The UNR multi-charged ion research facility.

2.2. The Beamline

Following charge-to-mass analysis, the ions travel about 2 m in the main ECR beamline before being guided to the new beamline by means of a 90° electrostatic deflector. A schematic of the new beamline is shown in Fig. 2. The beam may be focussed by an electrostatic quadrupole triplet lens, and x-y steered by a pair of Helmholtz coils. Several Faraday cups are installed to monitor, measure and optimize the beam current. If needed the ion beam may be collimated by means of a 4-jaw slit assembly and the collision chamber entrance aperture (variable size) which are 2.8 m apart. Three turbo-molecular drag pumps maintain a base pressure of about 5.0×10^{-9} torr in the beamline section leading to the collision chamber. In the differentially pumped collision chamber, a 6-inch cube, the ion beam will cross a target gas jet at 90°. The gas jet will be either an effusive one furnished by a glass capillary array, or a cryogenically cooled supersonic jet, depending on the experimental needs. For the experiments described in this thesis, an effusive jet was used.

During the experiments, the base pressure in the collision chamber will be in the 10^{-7}-10^{-6} torr range while the effective target pressure at the interaction region will be in the 0.1-10 mtorr.

Three of the six cube ports are available for the installation of the different apparatus needed for providing the target gas and detecting and characterizing the collision products other than the scattered projectiles. This includes the gas jet, the TOF recoil ion spectrometer and two-dimensional position sensitive microchannel plate detector

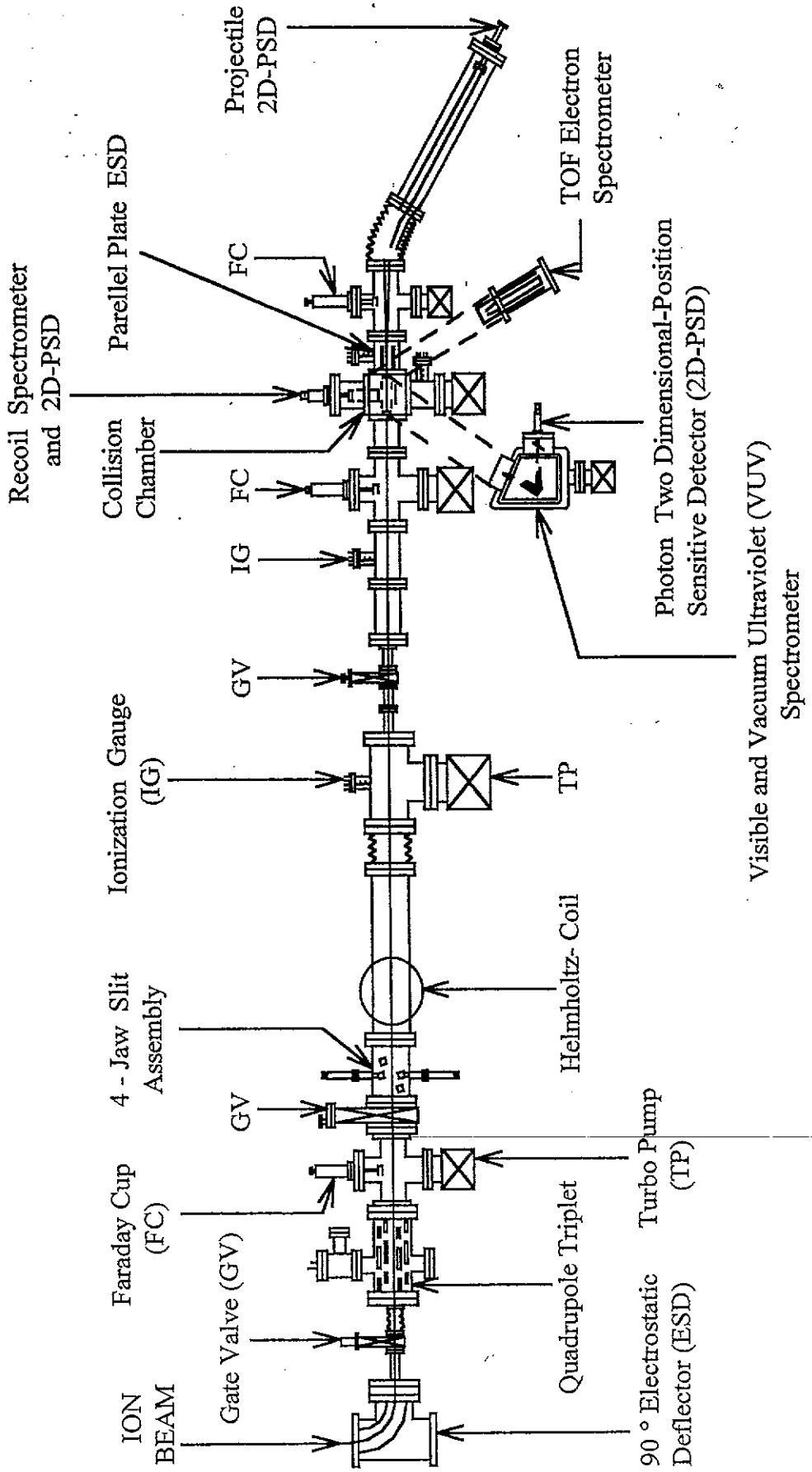

Figure 2. Schematic of the beamline.

(2D-PSD), the TOF electron spectrometer and the visible-VUV photon spectrometer. In addition, a light source and an electron gun may be installed for calibration and testing of the different spectrometers. After the collisions, the final projectile charge states are separated by a parallel plate electrostatic analyzer located immediately after the collision chamber exit and detected by a 2D-PSD. The exit region is maintained at a base pressure of about $8x10^{-9}$ torr. The beamline has been tested for beam transport and focusing in September, 1996, where He^{2+}, Ar^{8+} and O^{6+} ion beams have been admitted to the beamline and guided to the collision chamber. Typical ion beam currents measured at the second Faraday cup were 0.5-3.0 μA, while the current was about 40 nA at the third Faraday cup just after the collision chamber.

At the time this thesis was prepared, only the VUV-spectrometer was available for detecting collision products, and results from preliminary singles experiments will be presented and discussed in chapter 4.

2.3. The Photon Spectrometer and Detector

The photon spectrometer is an evacuable modified Seya-Namioka type monochromator [6] which was converted into a spectrometer by replacing the exit slit with a 2D-PSD. It utilizes a 0.2 meter (radius) concave holographic grating with 1200 grooves/mm which gives a reciprocal linear dispersion of 40 Å/mm in the first order.

The grating is iridium coated for enhanced reflectance in the extreme ultraviolet. The effective wavelength range covers the region from about 5000 Å to just below 300 Å. The spectrometer is mounted directly on the collision chamber.

A schematic of the photon detector is shown in Fig. 3. It consists of two microchannel plates (47 mm active diameter), in chevron assembly, and a Wedge and Strip position sensitive anode [7]. Since the detection efficiency of the channel plates drop rapidly for wavelength longer than 1200 Å, the front channel plate is coated with CsI, which extends the wavelength range to about 1800 Å while simultaneously increasing the overall detection efficiency from 10% to 25% over most of the effective range.

A potential difference of about 2 kV is maintained across the two channel plates while the anode is grounded. When a photon is incident at the input of a microchannel, secondary electrons are generated and multiplied until at the output a pulse of up to 10^7 electrons may be realized. The electron cloud then impinges on the position sensitive anode where the impact position along the dispersion axis (x-axis) determines the wavelength of the incident photon. At any one grating setting, the detector covers a range

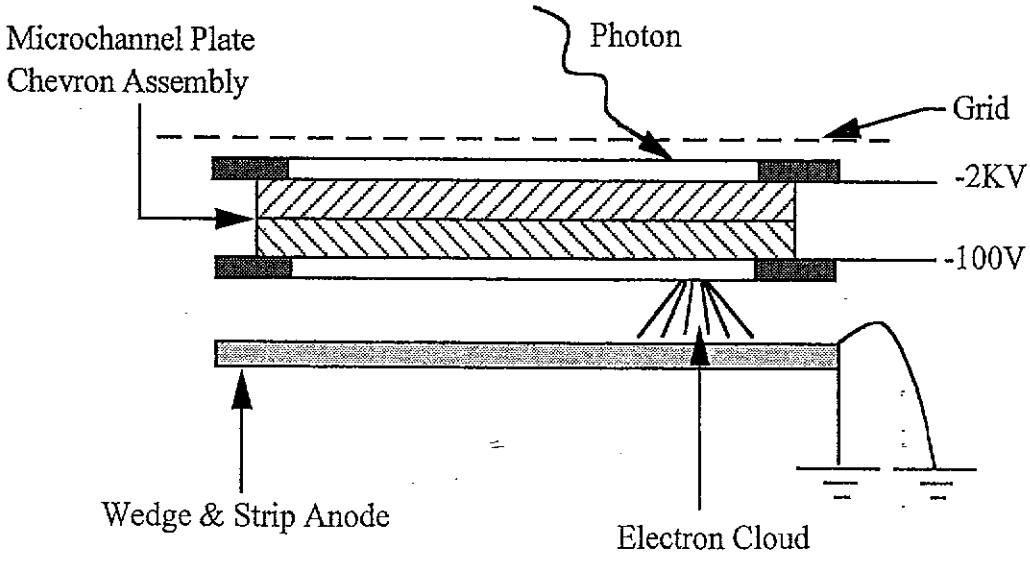

Fig. 3. Schematic of the microchannel plate detector.

of about 1200 Å centered at the spectrometer dial reading, which circumvents scanning normally required for monochromators while acquiring data.

The anode consists of three segments, the wedge (Y), the strip (X) and the meander (M) as shown in Fig. 4. When the electron cloud hits the anode, the total charge is shared by the three segments according to the segments areas exposed to the cloud. The position of each detected photon is determined, in principle, from the following charge ratios :

$$X = \frac{Q_x}{Q_x + Q_y + Q_m} \tag{1}$$

$$Y = \frac{Q_y}{Q_x + Q_y + Q_m} \tag{2}$$

However, since the different anode segments are capacitively coupled and since there exist void areas between the segments, a more elaborate procedure, which involves decoupling the individual signals and aspect ratio corrections, must be followed in order to obtain the actual (X,Y) position. Fig. 5. shows a two-dimensional image of the photon detector obtained by recording the signals produced by the dark current which has a typical rate of about 10 Hz. The uniformity of the image clearly demonstrates the absence of hot spots in the detector.

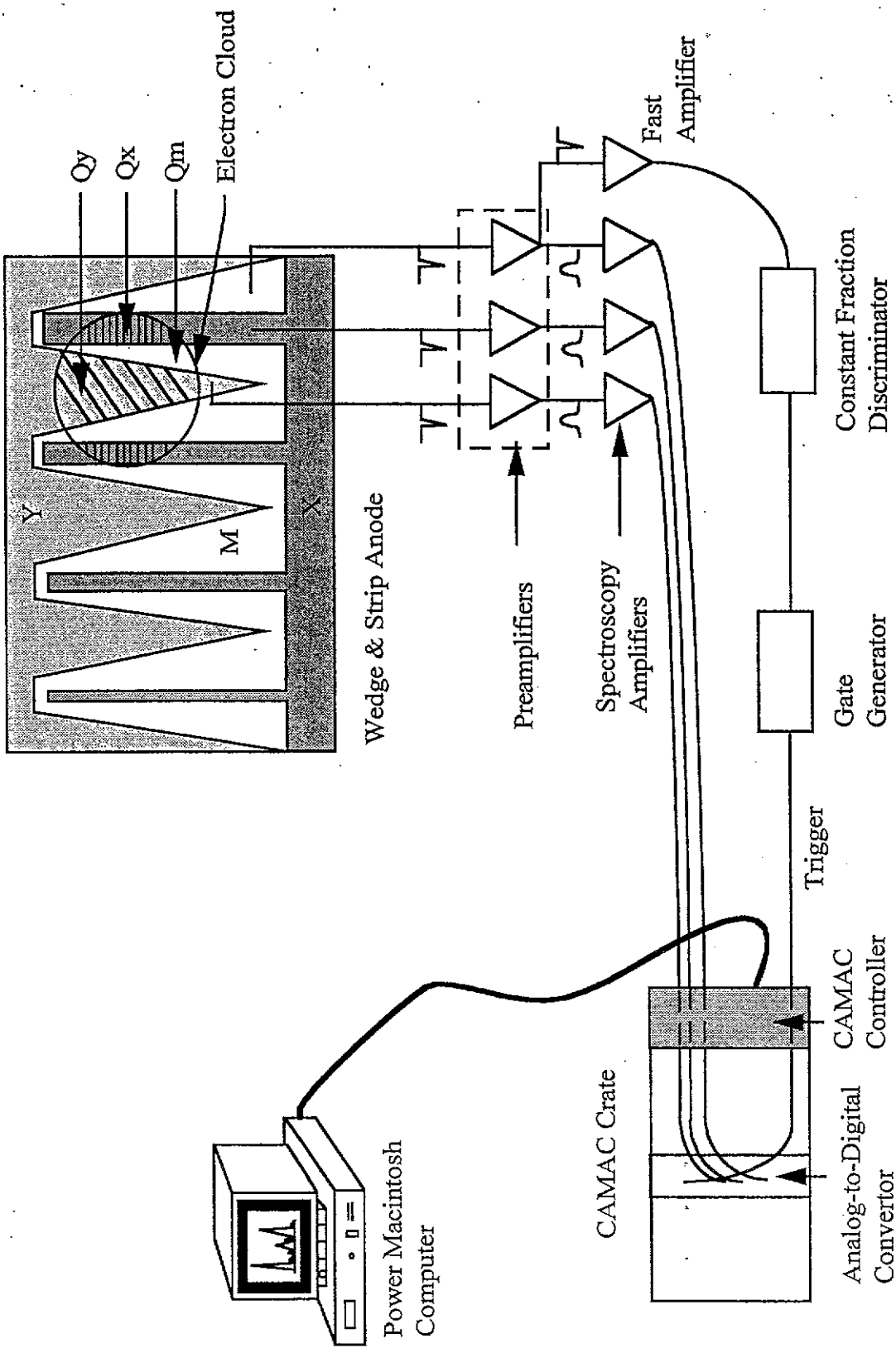

Figure 4. Schematic of the data acquisition system

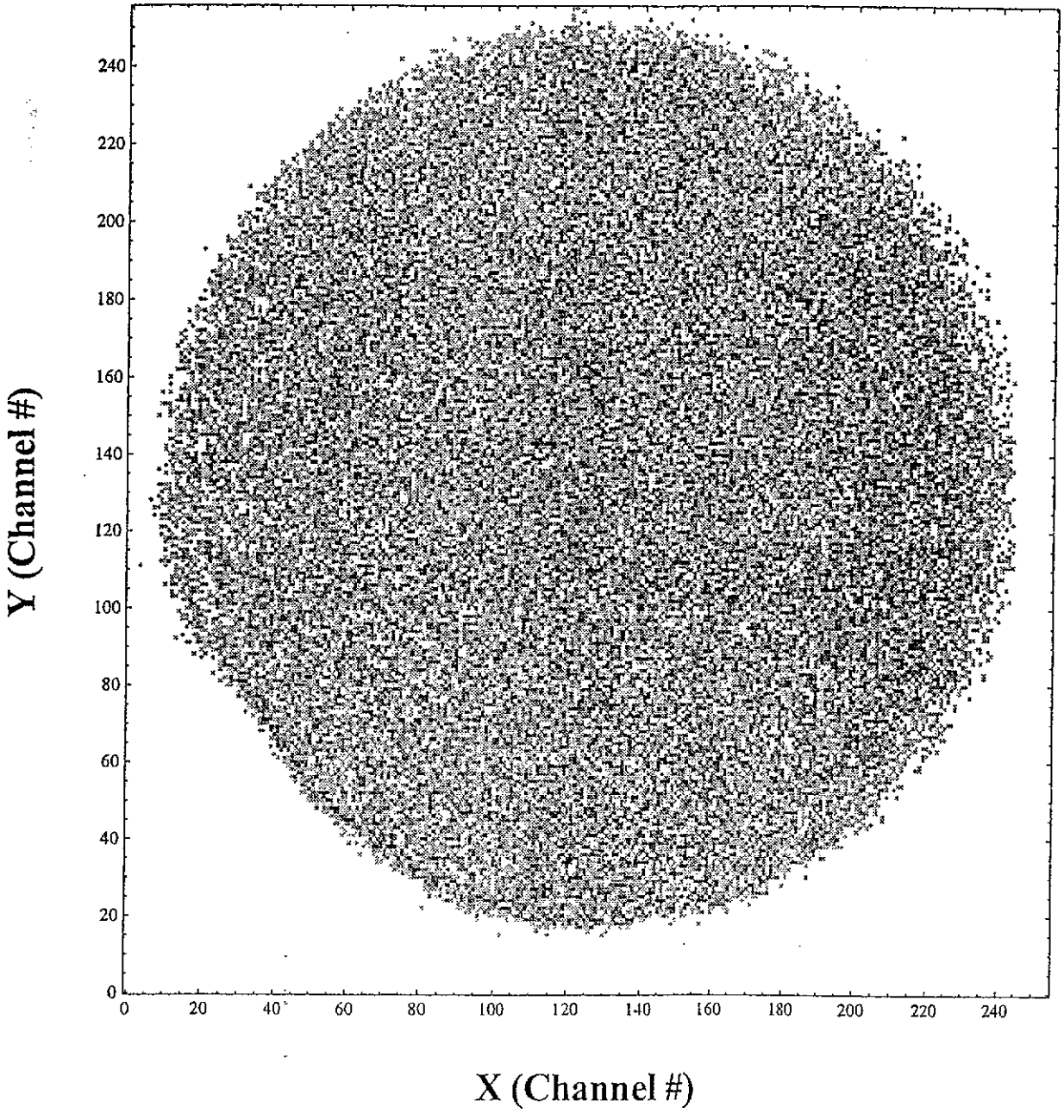

Fig. 5 : A two-dimensional image of the photon detector obtained by recording the dark current

2.4. The Data Acquisition System

The data acquisition system is a CAMAC based multi-parameter event-mode system which uses the Kmax software [8]. One of the major advantages of this system is the ability to store data in list-mode for future off-line analysis. In list-mode, all the parameters belonging to the same event are tagged as such and stored in raw form. Events are also processed on-line for immediate assessment of the data. Within the Kmax environment, conditions may be placed on individual or groups of parameters in order to increment one-dimensional histograms or two-dimensional scatter plots.

A schematic of the data acquisition system used in the present experiments is shown in Fig. 4. The charges appearing on the different anode segments are collected and processed by charge sensitive preamplifiers [9]. Each preamplifier has a slow output to be used for position encoding and a fast output for timing applications. The slow outputs are sent to spectroscopy amplifiers [10] for further processing and filtering, and the final signals are then sent to peak sensing analog-to-digital converters (ADC) [11].

One of the fast preamplifiers outputs is further processed by a fast amplifier [12] and a constant fraction discriminator (CFD) [13]. The output of the CFD is used to trigger a gate generator (GG) [14] which then produces a gate used to trigger the ADC's. For the position signals to be recorded and digitized they must arrive at the ADC's during the time the gate is applied. The digital signals are then passed by the CAMAC crate

controller [15] to the Power Macintosh computer, where the Kmax software recognizes the different signals as belonging to the same event. The raw data are then processed by the software as needed.

Fig. 6 shows an example of the raw pulse-height (PH) distributions for the parameters Q_x, Q_y and Q_m. When processed as described earlier these parameters give rise to the (X,Y) impact position of the particle or the position of a dark event as shown in Fig. 5.

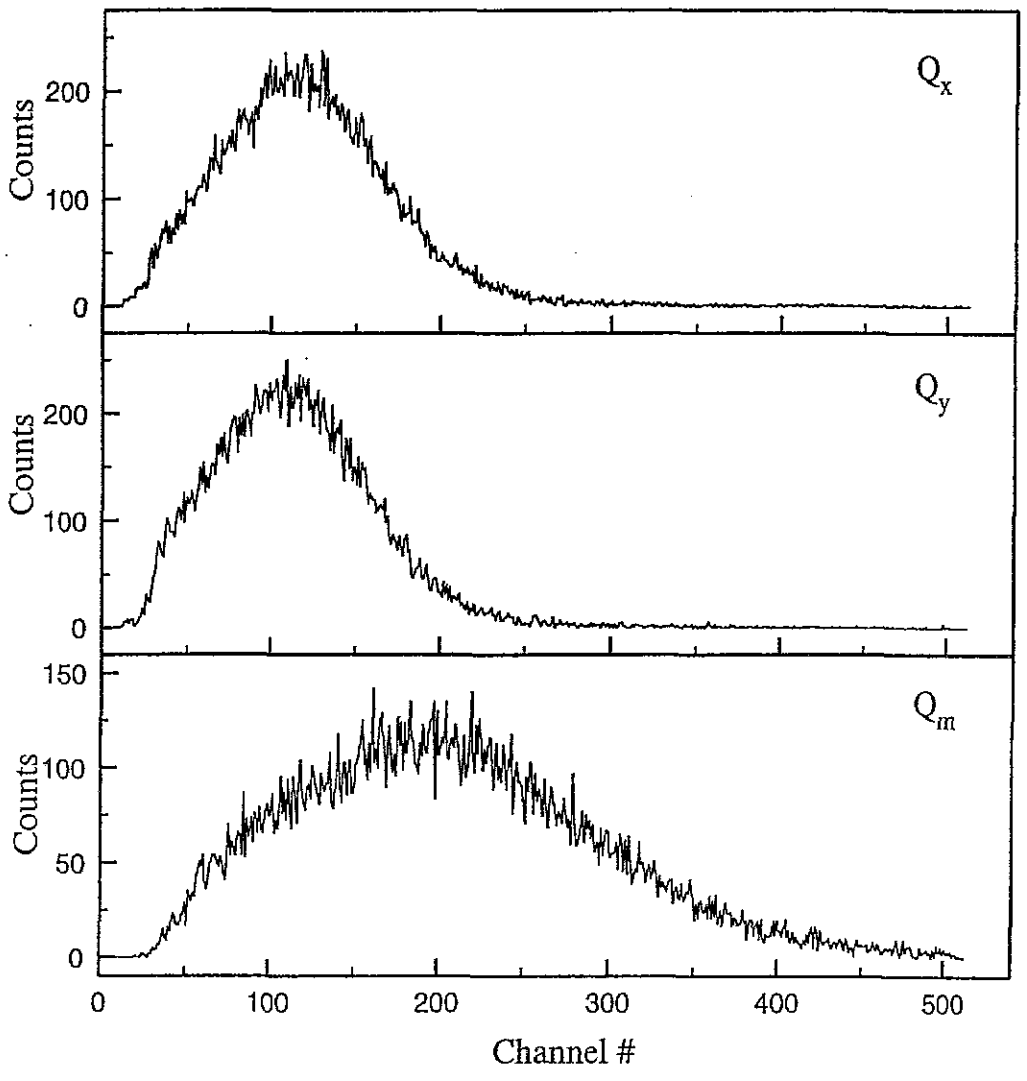

Fig. 6 : Raw pulse-height distributions for the parameters Q_x, Q_y and Q_m.

Chapter 3

Theoretical Considerations

Many of the processes occurring in slow ion-atom collisions may be understood in terms of the potential energy curves representing the entrance and different exit channels. Several models based on curve crossing have been developed to estimate cross sections for the processes involved, as well as predict Q-values and angular distributions. The classical over-barrier and Landau-Zener are such models.

3.1. Potential Energy Curves

The charge transfer process can be described using a graphic representation of the potential energy curves as a function of the internuclear distance R between the target and the projectile [16].

For simplicity, let us consider the system $A^{q+} + He$, where A^{q+} is a bare ion. If we neglect the polarization term (varies as $1/R^4$) in the expression for the potential energy, the system energy before the collision is given by

$$E_i = -B^{He}(1s) - B^{He^+}(1s) \qquad (3)$$

where the quantities $B^{He}(1s)$ and $B^{He^+}(1s)$ are respectively the first and second ionization energies of helium.

The final system energy is

$$E_f^{SC} = -B^{He^+}(1s) - E^{A^{(q-1)+}}(nl) + \frac{q_{A^{(q-1)+}} \cdot q_{He^+}}{R} \quad (4)$$

for single electron capture, and

$$E_f^{DC} = -B^{A^{(q-1)+}}(nl) - E^{A^{(q-2)+}}(n'l') + \frac{q_{A^{(q-2)+}} \cdot q_{He^{2+}}}{R} \quad (5)$$

for double electron capture. $E^{A^{(q-1)+}}(nl)$ and $E^{A^{(q-2)+}}(n'l')$ are the binding energies of the electrons in the configurations nl and n'l' respectively. The quantities $q_{A^{(q-1)+}}$ and $q_{A^{(q-2)+}}$ are respectively the charge for the ions $A^{(q-1)+}$ and $A^{(q-2)+}$. In the following E_i is taken as the zero energy.

Fig. 7 shows an example of the potential energy curves for the $C^{6+} + He$ collision system. The dotted lines represent the $C^{5+}(nl)$ orbitals, the solid line corresponds to the configuration *2l4l'* of C^{4+}. Within this picture, one may have a transition of an electron from one curve to another at the crossing points, i.e. when there is a resonance in energy. Hence, an electron is captured in the $C^{5+}(2l)$ orbital at roughly 2 a.u. when the entrance channel $C^{6+} + He$ crosses the single capture channel $C^{5+}(2l) + He^+$. The single capture in the other orbitals can happen in the same way. In addition, one may have a double electron capture to the configuration *2l4l'* in two steps. First, one electron is transferred to the *4l* orbital when the entrance channel $C^{6+} + He$ crosses that channel at about 23 a.u. The second electron is captured when the *4l* channel crosses the double capture channel $C^{4+} + He^{2+}(2l4l')$ at roughly 1.5 a.u.

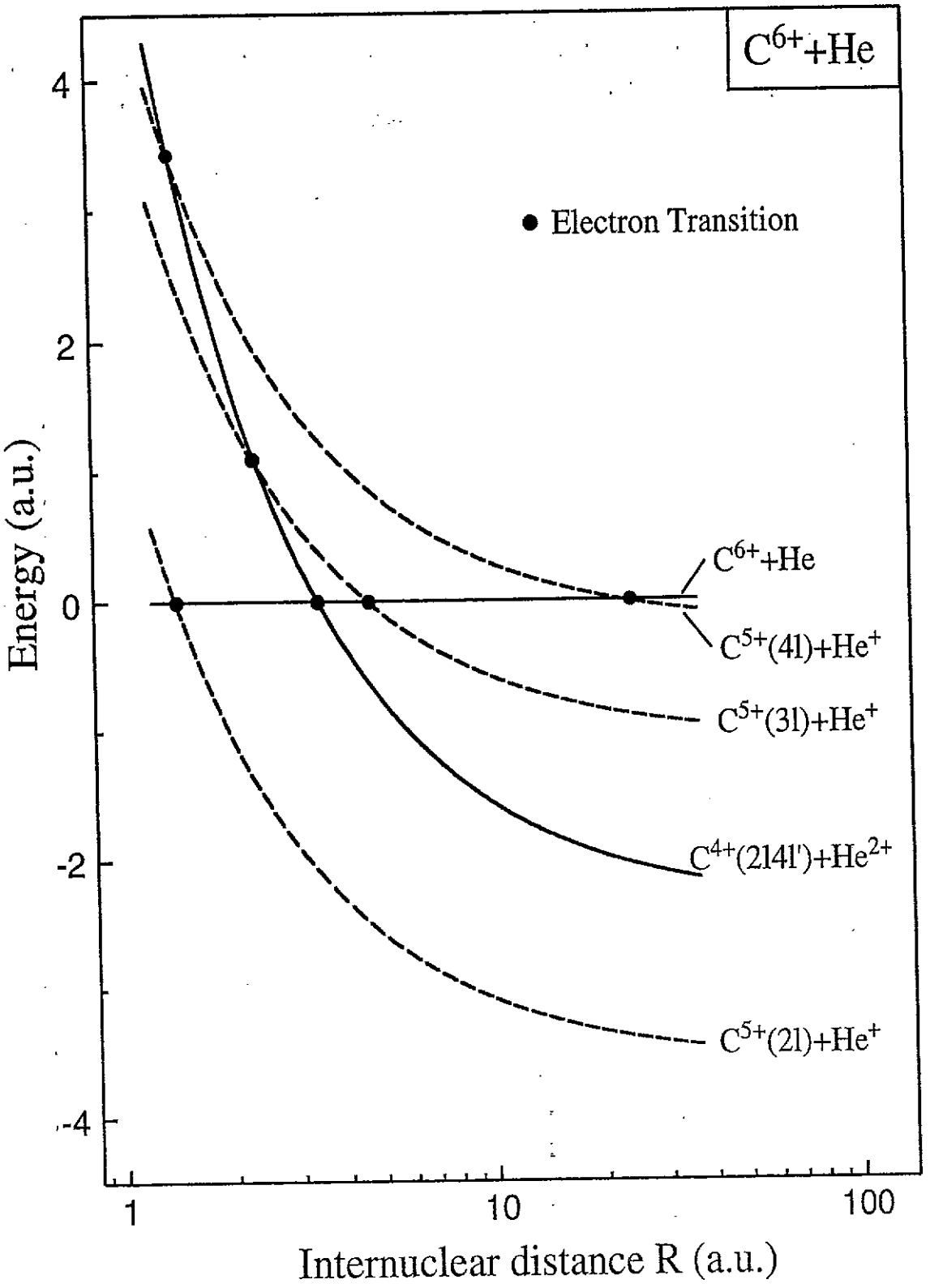

Fig. 7 : Potential energy curves for C^{6+} + He collisions.

3.2. The Classical Over-Barrier Model

The over-barrier model used by Ryufuku *at al.*[17] and extended by Niehaus [18] and Ba'ra'ny *et al.*[19] is a simple tool to estimate the cross section for electron capture by charged ions. The model implies that at a specific distance R_b an electron flows over the receding potential barrier with a high probability assuming that there are sufficient states at the other center.

Let us consider the system $A^{q+} + He$. To calculate the over-barrier distance, we start with the two-center coulomb potential of the charges q and q' determined without the active electron indicated in Fig. 8. Within the classical over-barrier model, The collision has two channels which are the entrance and exit channels. In the entrance channel, the active electron moves within the potential V(z) of the ions A^{q+} and $He^{q'+}$ ($q' = 1$ to 2) :

$$V(z) = V_{q'} + V_q = -\left(\frac{q'}{|z|} + \frac{q}{|R-z|}\right) \tag{6}$$

where R is the internuclear distance and z is the component of the position vector of the electron along the axis passing through the two point charges q and q' with its origin at q' (see Fig. 8). The distance z_m , where the combined potential has a local maximum, is obtained by setting the derivative equal to zero :

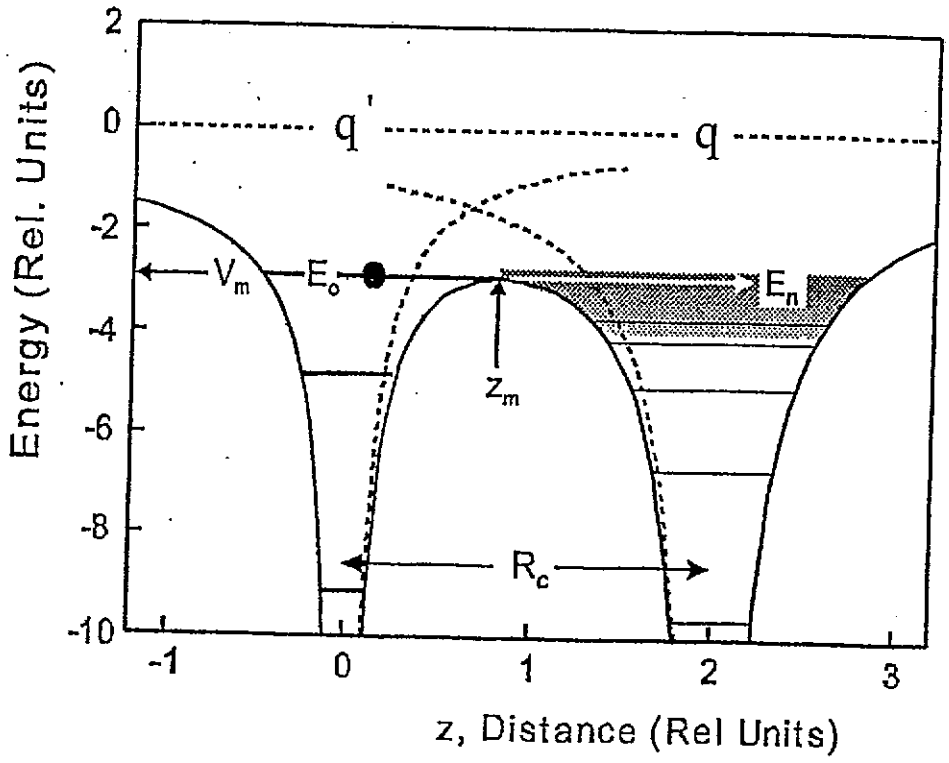

Fig. 8 : Schematic diagram of the energy and distance in the classical over-barrier model

$$\frac{dV}{dz} = \frac{q'}{z_m^2} + \frac{q}{(R - z_m)^2} = 0 \tag{7}$$

Solving the associated quadratic equation one gets

$$z_m = R\frac{\sqrt{q'}}{\sqrt{q} + \sqrt{q'}} \tag{8}$$

As expected $z_m \to 0, R/2, R$ for $q' \to 0, q' \to q$, and $q \to 0$, respectively. The maximum value for the potential V_m is obtained by substituting z_m in Eq. (6). After some manipulation it follows that

$$V_m = -\frac{\left(\sqrt{q'} + \sqrt{q}\right)^2}{R} \tag{9}$$

The electronic state at the left center with charge q' has the asymptotic energy E_0. When the other charge q is approaching, the electronic state is lowered according to $E_0(z) = -(E_0 + q/R)$. The electron starts to flow to the other center when the barrier potential V_m becomes equal to the energy $E_0(z)$. This condition determines the over-barrier distance R_b

$$E_0 + \frac{q}{R_b} = \frac{\left(\sqrt{q'} + \sqrt{q}\right)^2}{R_b} \tag{10}$$

Solving for R_b it follows that

$$R_b = \frac{q' + 2\sqrt{q'.q}}{E_0} \tag{11}$$

Likewise one obtains the potential

$$V_m = E_0 \frac{\left(\sqrt{q'} + \sqrt{q}\right)^2}{q' + 2\sqrt{q'.q}} \tag{12}$$

A condition for resonant charge transfer is that the energies of the states on either center, modified by the Coulomb potential of the other center, are equal, i.e,

$$E_0 + \frac{q}{R_c} = E_n + \frac{q'}{R_c} \tag{13}$$

where R_c is the crossing radius for the associated states. Recall that the charges are determined without the active electron. Equation (13) can be solved with regard to the crossing radius

$$R_c = \frac{q - q'}{E_n - E_0} \tag{14}$$

There are two necessary conditions for the over-barrier transfer of the electrons formulated by Eqs. (11) and (14). The distance at which this transfer starts is given as the minimum of the distance R_b and R_c

$$R_m = \min(R_b, R_c) \tag{15}$$

The corresponding cross section is given by its geometric value as

$$\sigma_c = p_c \pi R_m^2 \tag{16}$$

where p_c is the charge transfer probability.

The essential characteristics for the over-barrier model is the presence of closely lying states E_n in which the electron can exist after overcoming the receding barrier. In this case, the distances are approximately equal, i.e., $R_c \approx R_b$. Moreover, the probability p_c for charge transfer is set to its maximum value ranging from ~ 0.5 to 1.

In particular, the specific state into which the electron is transferred by the over-barrier mechanism is determined from Eq. (14) replacing R_c by R_b

$$E_n = E_0 + \frac{q - q'}{R_c} = E_0\left(1 + \frac{q - q'}{q' + 2\sqrt{q'.q}}\right) \tag{17}$$

If the state at the center q refers to a Rydberg electron, whose principal quantum number is n, its energy can be approximated by $E_n = q^2/2n^*$, where $n^* = n\text{-}\Delta$ and Δ is the quantum defect. Then the quantum number of the populated Rydberg state is given by

$$n^{*} = \frac{q}{\sqrt{2E_0\left(1+\frac{q-q'}{q'+2\sqrt{q'.q}}\right)}} \qquad (18)$$

3.3. The Landau-Zener Model

In this model [20], the motion of the nucleus is treated classically and separated from the electrons motion. In addition one assumes that :

i) the transitions occur at the crossing points of the electronic states.

ii) the electronic states are constant within the pseudocrossing regions δR of the internuclear distance R.

iii) the rotational coupling is not taken into account.

Within the above assumptions, the electronic Hamiltonian matrix for a two state system can be written as:

$$H_{el} = \begin{bmatrix} H_{11}(R) & H_{12}(R) \\ H_{21}(R) & H_{22}(R) \end{bmatrix} = \begin{bmatrix} E(R_c)+\frac{\Delta F_{12}}{2}(R-R_c) & H_{12}(R_c) \\ H_{12}(R_c) & E(R_c)+\frac{\Delta F_{12}}{2}(R-R_c) \end{bmatrix} \qquad (19)$$

where R_c is the internuclear distance in the vicinity of the curve crossing (Fig 9), where $E(R_c)$ can be expressed as

$$E(R_c) = H_{11}(R) = H_{22}(R_c), \qquad (20)$$

and $H_{12}(R_c)$ is the exchange term. Furthermore we can define

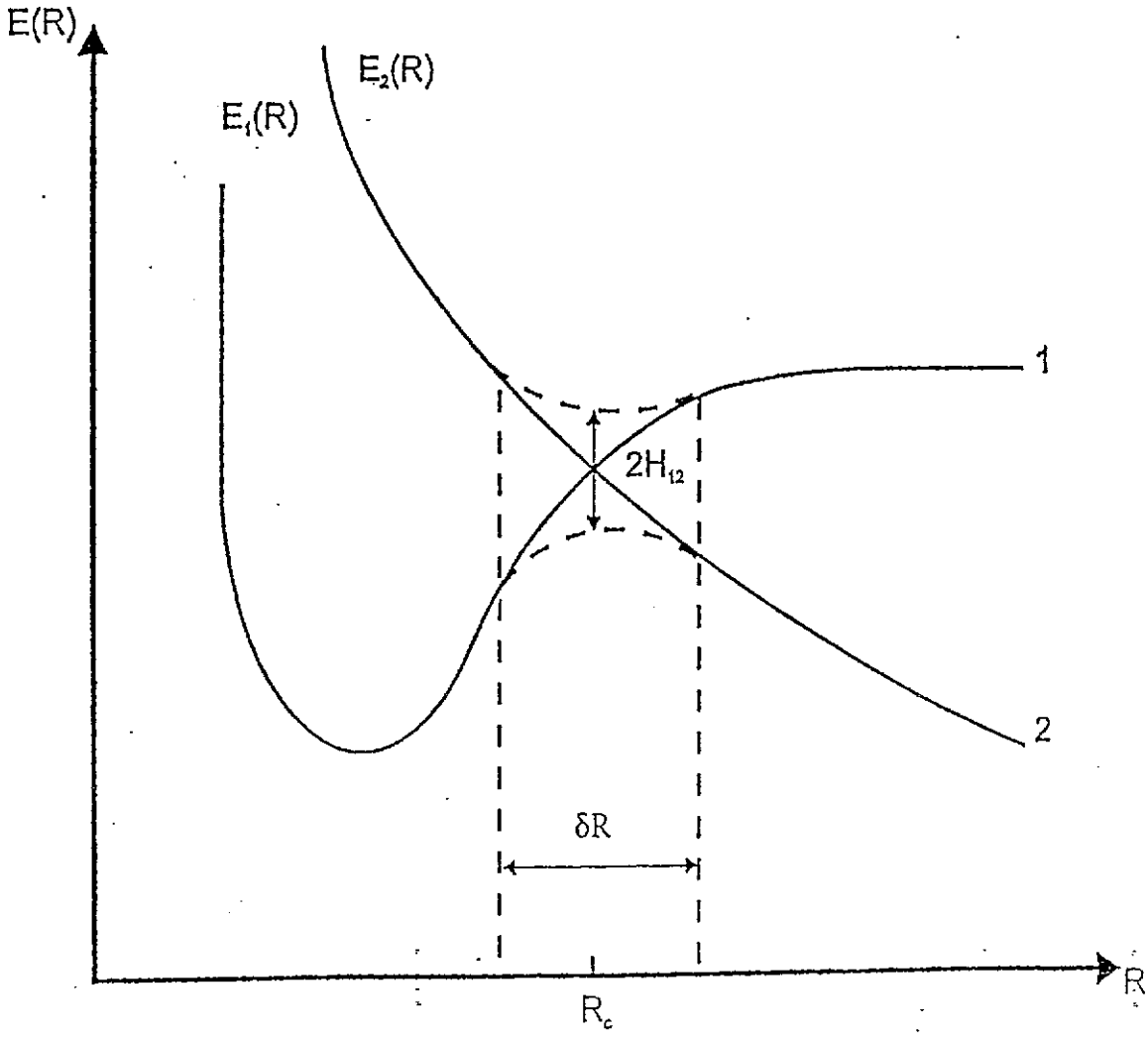

Fig. 9: Schematic crossing of the potential energy curves in the Landau-Zener Model.

$$\Delta F_{12} = \frac{d}{dR}\left|H_{11}(R) - H_{22}(R)\right|_{R=R_c} \qquad (21)$$

where ΔF_{12} is a measure for the relative slopes of the potential curves at the crossing point R_c

The probability of a "single electron transition" at R_c, i.e, form channel 1 to channel 2, can be described by

$$p_{12} = \exp\left[-\frac{2\pi H_{12}^2(R_c)}{\Delta F\ v_{rad}}\right] \qquad (22)$$

where v_{rad} is the radial velocity,

$$v_{rad} = v\sqrt{1-\frac{b^2}{R_c^2}}\ , \qquad (23)$$

b is the impact parameter and v is the projectile velocity.

The term H_{12} can be evaluated using the following formula provided by Olson and Salop [21] :

$$H_{12} = \frac{9.13}{\sqrt{q}}\exp\left[-1.324R_c\sqrt{\frac{2B^{He}(1s)}{q}}\right] \qquad (24)$$

In equation (24), $B^{He}(1s)$ is the first ionization energy of helium and q the projectile charge.

The crossing is traversed twice, once while the collision partners are approaching each other and once while receding from each other. Therefore, the total transition probability for single capture can be written as :

$$P_{12} = 2p_{12}(1-p_{12}) \qquad (25)$$

In Eq (25) the total probability P_{12} is obtained by summing over the different path ways from the entrance channel to the single electron capture channel corresponding to the probability p_{12} and $(1-p_{12})$.

Finally, the cross sections are then given by :

$$\sigma_{sc} = \int_0^{R_c} P_{12} 2\pi b \, db \tag{26}$$

For example, in 90 keV C^{6+}+He collisions,single electron capture into the n=3 shell occurs at a crossing radius of 4.56 a.u. and the corresponding cross section is $\sigma_{sc}= 3.79\text{x}10^{-15}\text{cm}^2$.

Chapter 4

Experimental Results and Discussion

The first experiments carried out at the new beamline are associated with electron capture and target excitation in slow collisions of multiply charged ions with many-electron targets. These experiments utilized the VUV-spectrometer described earlier in section 2.3.

Electron capture is usually the dominant process in such collision while target excitation is expected to be a much weaker process. So far, very little is known about the latter process since the state selective target excitation studies in slow collisions are generally rather difficult. Thus, Cederquist [22] analyzed low-energy data on single and double electron removal from the target in Xe^{q+} - He collisions within the classical over-barrier model and found indications for contributions of the transfer excitation process. Moreover, Cederquist and co-workers [23] have also extended the classical over-barrier model to account for target excitation. In their model, they describe the mechanism of target excitation as a three-step process where one electron is first transferred to the projectile at the internuclear distance R_1, the other target electron is then transferred to the projectile at the internuclear distance R_2. As the radial turning point is approached, the most tightly bound of the two Rydberg electrons is transferred further to quasi-molecular states associated with recapture to an excited target state.

An investigation of O^{6+} and N^{6+} collisions with He at 9 keV using the method of energy-gain spectroscopy [24] has also shown a small peak which was attributed to

transfer-excitation. Recently it has been found in calculations [25] and in measurements [26,27] that in the case of slow He^{2+} - He collisions, transfer-excitation cross sections can be about as large as the corresponding cross sections for single electron transfer (which in turn are smaller than the two-electron transfer cross sections in this system). Fritsch [28] carried out calculations for the transfer-target excitation process in C^{6+} + He collision system and showed that it is more than one order of magnitude smaller than single electron capture.

In the following, we discuss our first results for the collision systems O^{6+} + He and O^{6+} + Ar. Although we are mainly concerned with atomic targets, we have actually started our investigations by investigating the $He^{2+} + N_2$ collision system as a bench mark test of our setup. The richness of the spectra obtained for He^{2+} + N_2 prompted us to obtain spectra for electron impact on N_2 for comparison.

4.1. $He^{2+} + N_2$ and $e^- + N_2$ Collisions

In these studies, 20 keV He^{2+} ions were extracted from the ECR ion source and a beam current of 3 μA has been measured in the second Faraday cup just before the collision chamber entrance. The entrance aperture diameter was 1 mm. During the course of this experiment, the third Faraday cup after the collision region was not installed yet, which made it rather difficult to optimize the beam size and overlap with the jet since we had to rely on the spectrometer photon detector count rate for ion beam optimization. Therefore we do not know the beam portion actually crossing the target jet.

Nevertheless, first VUV spectra have been obtained at different grating settings. As an example, we show in Fig. 10 a spectrum obtained at a grating setting centered at 1085 Å.

We also show in Fig. 10 a spectrum resulting from $e^- + N_2$ collisions at the same grating setting. The electrons have been produced by a 2 kV cold cathode discharge, where the discharge chamber was about 1 m from the spectrometer entrance slit.

Since the photon detector is a two-dimensional position sensitive detector, the spectra in Fig. 10 were obtained by projecting the two-dimensional scatter plots onto the dispersion axis (X-axis). The scatter plot corresponding to the $e^- + N_2$ spectrum of Fig. 10 is shown in Fig. 11. In such a plot the darkness of the lines reflect their relative intensities. We note that the lines are slightly curved which is a consequence of the imaging properties of the concave grating.

The curvature of the lines causes a slight deterioration of the wavelength resolution which can be eliminated by means of linearization procedures. In this work, however, we have chosen to project only those photon events lying within the rectangular window displayed in Fig. 11. This presudure slightly improved the resolution and the signal-to-dark count ratio. In our study the resolution was limited mainly by the position resolution of the detector which was about 0.35 mm corresponding to about 14 Å. The spectrometer entrance slit width was 0.25 mm which gave rise to a net full width at half maximum (FWHM) of about $\Delta\lambda = 17$ Å.

We now discuss the spectra shown in Fig. 10.The prominent lines in both spectra are labeled and identified in tables 1 and 2. For the $He^{2+} + N_2$ system the

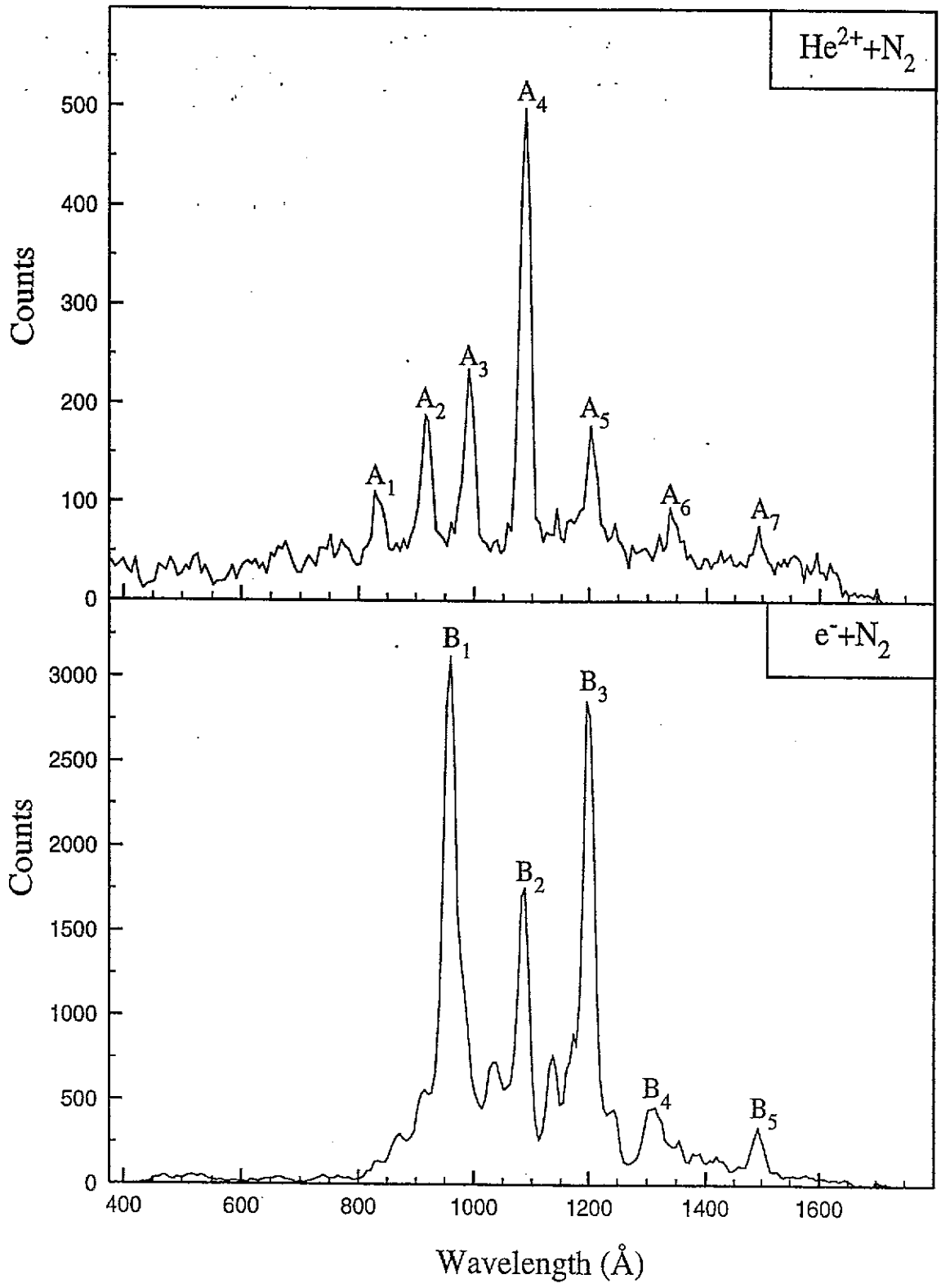

Fig. 10 : Spectra obtained in $He^{2+} + N_2$ and $e^- + N_2$ collisions. The spectra are centered at 1085 Å. See table 1 and 2 for identification of the prominent lines.

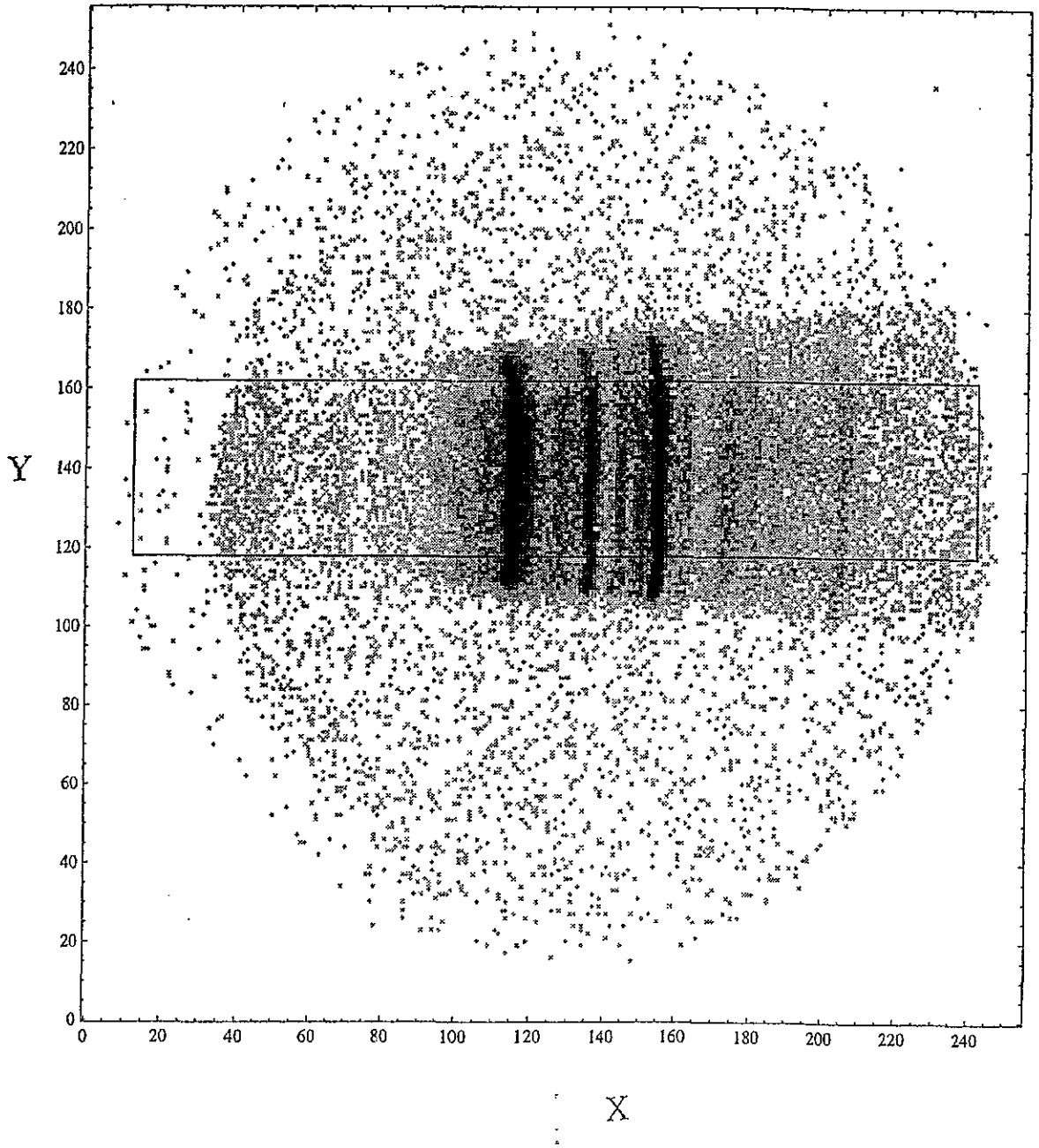

Fig. 11 : A two-dimensional scatter plot of VUV radiation observed in e^-+N_2 collisions at a grating dial setting of 1085Å

Table 1 : Experimental wavelengths observed in $He^{2+} + N_2$ collisions (Fig. 10). Line identification is obtained from the tabulation by Kelly [29]. The associated transitions and the radiating species are also given.

Label	Wavelengths (Å)	Transition Initial state-Final state	Radiating Species
A_1	≈ 836	$2s\ 2p^2\ (^4P)\ 3s - 2s\ 2p^3$	N^+
A_2	915.6	$2s2p^3\ ^3P_1 - 2s^2 2p^2\ g\ ^3P_0$	N^+
	916.0	$2s2p^3\ ^3P_2 - 2s^2 2p^2\ g\ ^3P_1$	N^+
	916.7	$2s2p^3\ ^3P_1 - 2s^2 2p^2\ g\ ^3P_2$	N^+
A_3	992.3	$7p\ ^2P_{3/2} - 2s\ ^2S_{1/2}$	He^+
	992.4	$7d\ ^2D_{5/2} - 2p\ ^2P_{3/2}$	He^+
	991.6	$2s2p^2\ ^2D_{5/2} - 2s^2 2p\ g\ ^2P_{3/2}$	N^{2+}
A_4	1084.9	$5p\ ^2P_{3/2} - 2s\ ^2S_{1/2}$	He^+
	1085.0	$5d\ ^2D_{5/2} - 2p\ ^2P_{3/2}$	He^+
	1084.6	$2s2p^3\ ^3D_2 - 2s^2 2p^2 g\ ^3P_1$	N^+
	1085.5	$2s2p^3\ ^3D_2 - 2s^2 2p^2\ g\ ^3P_2$	N^+
	1085.7	$2s2p^3\ ^3D_3 - 2s^2 2p^3\ g\ ^3P_2$	N^+
A_5	1199.5	$2s^2 2p^2 3s\ ^4P_{5/2} - 2s^2 2p^3\ g\ ^4S_{3/2}$	N
	1200.2	$2s^2 2p^2 3s\ ^4P_{3/2} - 2s^2 2p^3\ g\ ^4S_{3/2}$	N
	1200.7	$2s^2 2p^2 3s\ ^4P_{1/2} - 2s^2 2p^3\ g\ ^4S_{3/2}$	N
A_6	≈ 1324 - 1355		N, N^+, N^{2+}
A_7	1492.6	$2s^2 2p^2 3s\ ^2P_{3/2} - 2s^2 2p^3\ ^2D_{5/2}$	N
	1492.8	$2s^2 2p^2 3s\ ^2P_{3/2} - 2s^2 2p^3\ ^2D_{3/2}$	N
	1494.7	$2s^2 2p^2 3s\ ^2P_{1/2} - 2s^2 2p^3\ ^2D_{3/2}$	N

Table 2 : Experimental wavelengths observed in $e^- + N_2$ collisions (Fig. 10) Line identification is obtained from the tabulation by Kelly [29] and Ajello *et al.* [30]. The associated transitions and the radiating species are also given.

Label	Wavelengths (Å)	Transition Initial state -Final state	Radiating Species
B_1	≈ 958		N_2
	955.3	$2p^2\ ^1S_0 - 2s2p\ ^1P_1$	N^{3+}
B_2	≈ 1083.3		N_2
	1084.6	$2s2p^3\ ^3D_2 - 2s^22p^2\ g\ ^3P_1$	N^+
	1085.5	$2s2p^3\ ^3D_2 - 2s^22p^2\ g\ ^3P_2$	N^+
	1085.7	$2s2p^3\ ^3D_3 - 2s^22p^3\ g\ ^3P_2$	N^+
B_3	1199.5	$2s^22p^23s\ ^4P_{5/2} - 2s^22p^3\ g\ ^4S_{3/2}$	N
	1200.2	$2s^22p^23s\ ^4P_{3/2} - 2s^22p^3\ g\ ^4S_{3/2}$	N
	1200.7	$2s^22p^23s\ ^4P_{1/2} - 2s^22p^3\ g\ ^4S_{3/2}$	N
B_4	1310.5	$2s^22p^23d\ ^2D_{5/2} - 2s^22p^3\ ^2P_{3/2}$	N
	1310.9	$2s^22p^23d\ ^2D_{3/2} - 2s^22p^3\ ^2P_{1/2}$	N
B_5	1492.6	$2s^22p^23s\ ^2P_{3/2} - 2s^22p^3\ ^2D_{5/2}$	N
	1492.8	$2s^22p^23s\ ^2P_{3/2} - 2s^22p^3\ ^2D_{3/2}$	N
	1494.7	$2s^22p^23s\ ^2P_{1/2} - 2s^22p^3\ ^2D_{3/2}$	N

majority of the lines are associated with either transitions arising from neutral nitrogen atoms (N) or singly charged ions (N^+). Since single electron capture is the dominant process in slow collisions, we believe that the excited species N and N^+ must have originated from the dissociation of excited N_2^+ following electron capture by He^{2+}. Such processes are clearly transfer-target excitation processes. However, since the target is molecular, the excitation mechanisms are not easily compared to those of atomic targets and we refrain from discussing such mechanisms in this work.

Two of the lines, A_3 and A_4, are shared by He^+ and N^{2+} and N^+ ions respectively. In He^+ they correspond to the transitions 7p→2s and 5p→2s respectively. However, the 7p and 5p states decay with about 80 % of the total transition probability to the 1s level. Furthermore, electron capture by He^{2+} ions is expected to dominantly proceed to low lying projectile states (n) with the capture probability decreasing with increasing n. Therefore, if lines A_3 and A_4 have substantial contributions from He^+ (np→2s) transitions we would also expect a strong line between A_3 and A_4 at 1025 Å resulting from 6p→2s transition in He^+. No such line is observed and therefore we argue that A_3 and A_4 are dominated by N^{2+} and N^+ transitions respectively. In fact, we have also searched for the 304 Å line corresponding to 2p→1s transition in He^+, we could not however identify this line. The reason behind this is probably caused by the fact that the VUV-spectrometer efficiency decreases rapidly for wavelengths below 300 Å and is already quite low for the 304 Å line.

For the $e^- + N_2$ collision system, the lines in Fig. 10 are identified in table 2. Many of the lines are common to both $e^- + N_2$ and $He^{2+} + N_2$. A marked difference is line B_1 which has no counterpart in the $He^{2+} + N_2$ spectrum. This line has been identified to originate from excited N_2 molecules and possibly N^{3+} ions. Ajello et al. [30] have shown that electron impact on N_2 induces strong molecular emission lines centered at 958 Å. Although their electron energies ranged from 10 - 400 eV while in our case it was 2 keV, the similarity in the relative intensities of lines B_1, B_2 and B_3 in both their and our measurements favors that line B_1 be attributed to molecular emission. While line B_2 may

also have contributions from molecular emission, James et al. [31] have shown that it is dominated by N^+ emission for electron energies higher than about 50 eV.

To remove the ambiguities associated with the spectrum for the He^{2+} + N_2 system, we plan to carry out similar investigations for the system He^{2+} + Ar, where the number of outer-shell electrons and binding energies are close to those of N_2 but molecular effects will be absent.

4.2. O^{6+} + He and O^{6+} + Ar Collisions

The system O^{6+} + He has been investigated by Roncin et. al. [24] at 9 keV and by Dijkkamp et. al. [32] at different energies. In addition to the dominant electron capture processes, Roncin et. al. have identified a transfer-target excitation peak with a cross section of 1.5×10^{-17} cm^2 which amounted to only 1.8% of the single capture cross section.

We have investigated the same collision system at 78 keV collision energy. A current of 35 nA of O^{6+} was measured on the third Faraday cup just after the collision chamber. Figures 12 and 13 show the obtained spectra at grating dial settings of 500Å and 1215Å. The various lines are identified in table 3. The only identifiable lines are those originating from 4f→3d and 2p→2s in O^{5+}. We do not see any evidence of the He^+ residual target excitation giving rise to transitions at 304 Å (n=2→n=1).

While such excitation takes place as observed by the aforementioned investigators, the small cross section clearly does not enable us to distinguish them from the dark current background seen in the spectra.

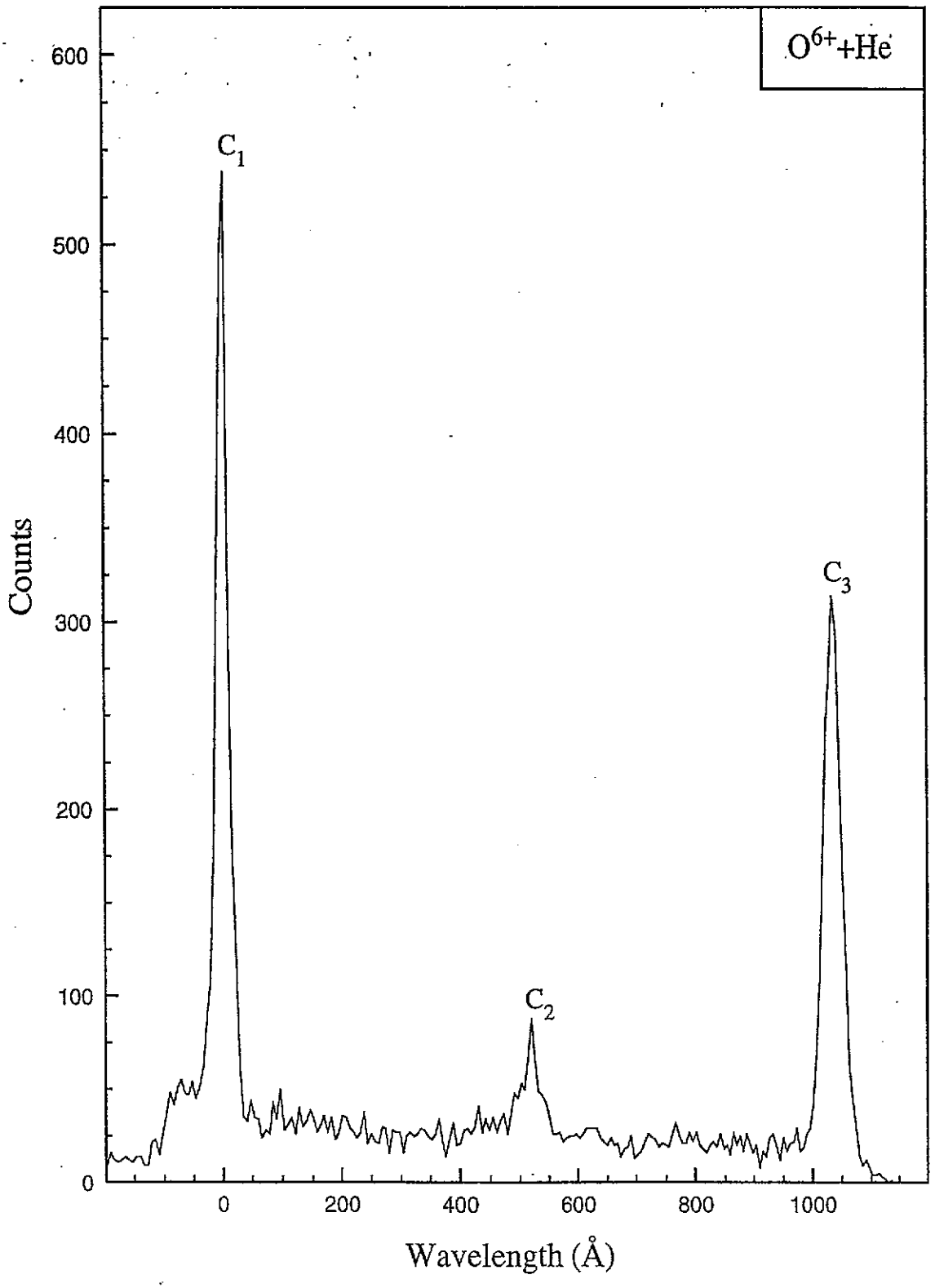

Fig. 12 : Spectrum obtained in O^{6+} + He collision. The spectrum is centered at 500 Å. See table 3 for identification of the prominent lines.

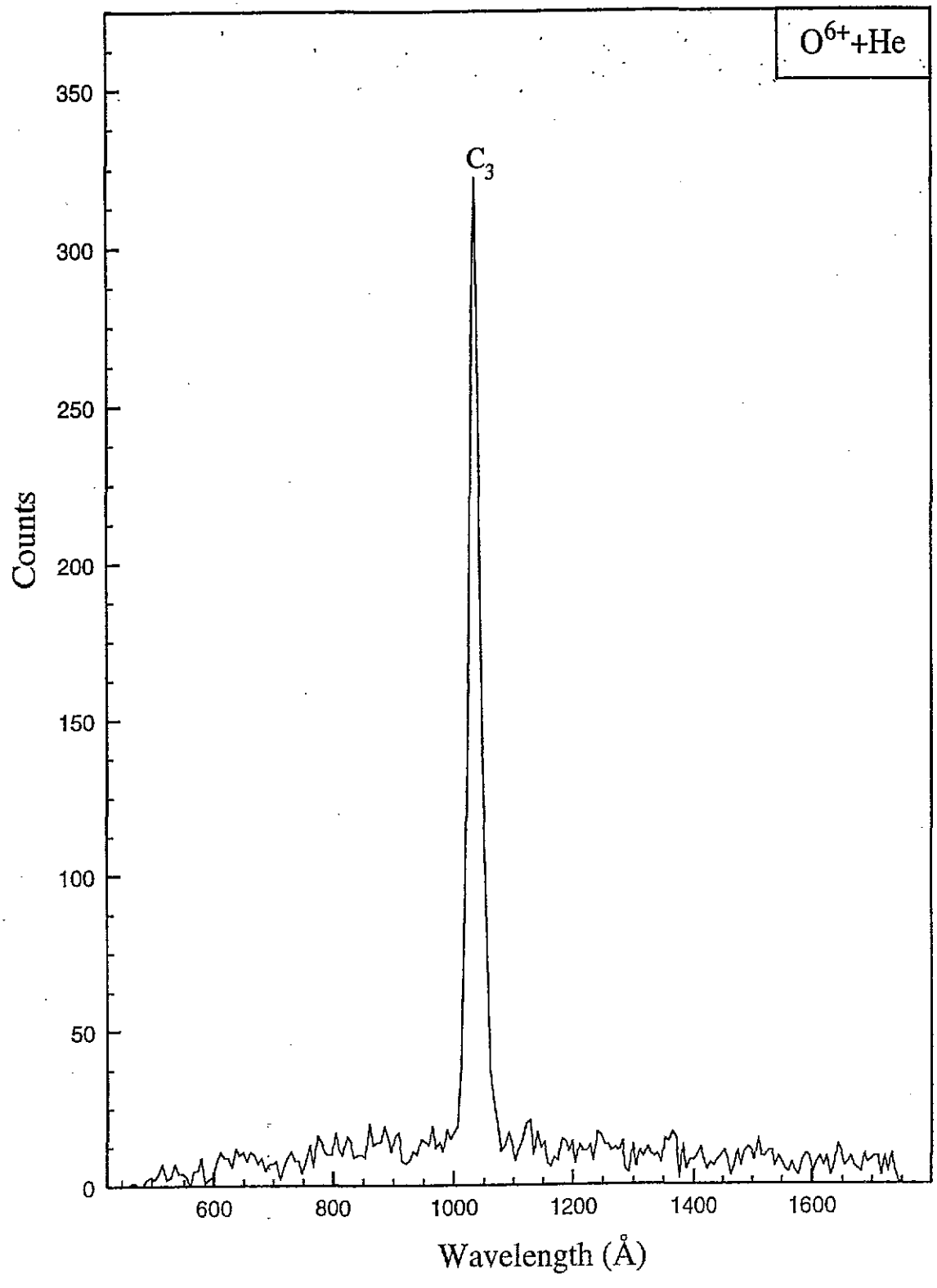

Fig. 13 : Spectrum obtained in O^{6+} + He collision. The spectrum is centered at 1215 Å. See table 3 for identification of the prominent lines.

Table 3 : Experimental wavelengths observed in O^{6+} + He collisions (figures 12 and 13) Line identification is obtained from the tabulation by Kelly [29]. The associated transitions and the radiating species are also given.

Label	Wavelengths (Å)	Transition Initial state-Final state	Radiating Species
C_1	Zero-order		
C_2	519.6	$1s^2 4f\ ^2F_{5/2} - 1s^2 3d\ ^2D_{3/2}$	O^{5+}
	519.7	$1s^2 4f\ ^2F_{5/2} - 1s^2 3d\ ^2D_{7/2}$	O^{5+}
	498.4	$1s^2 4d\ ^2D_{5/2} - 1s^2 3p\ ^2P_{3/2}$	O^{5+}
C_3	1031.9	$1s^2 2p\ ^2P_{3/2} - 1s^2 2s\ g\ ^2S_{1/2}$	O^{5+}
	1037.9	$1s^2 2p\ ^2P_{1/2} - 1s^2 2s\ g\ ^2S_{1/2}$	O^{5+}

To identify such processes, the signal-to-dark current ratio must be improved. Future measurements should involve higher beam current intensities and enhanced photon collection efficiency by means of a glass-capillary-converter (GCC) [33].

Line C_2 has been identified as 4f→3d and 4d→3p transitions while C_3 represents 2p→2s transition in O^{5+}. Other measurements [24,32] have shown that capture to n=2 is negligible, and therefore the high intensity of line C_3 is attributed to cascades from 4s, 4d, 3s and 3d levels to the 2p level.

We have attempted to compare the experimental intensity ratio of line C_2 to line C_3 with the ratio one would obtain from the predictions of the Landau-Zener model combined with a cascade scheme. However, the Landau-Zener cross section predictionsfor single electron capture to n = 3 and n = 4 are $\sigma_{n=3} = 3.58 \times 10^{-15}$ cm^2 and $\sigma_{n=4} = 9.15 \times 10^{-21}$ cm^2. $\sigma_{n=3}$ is about six orders of magnitude larger than $\sigma_{n=4}$ which is in clear contradiction with the experimental observation. For comparison, we show in

figures 14 and 15 the results of recent measurements by Phaneuf et.al. [34] for 60 keV O^{6+} + He using high resolution grazing-incidence monochromator. In Fig. 14 the small peak labeled 9 is identified as resulting from 2p→1s transitions in He^{+} which is a signature of transfer-excitation. Interestingly, a group of lines (1-4) centered at about 299 Å are identified as originating from O^{5+} ions. These lines were not observed in our spectrum which may indeed be an indication of a very low grating reflectance in our spectrometer at these wavelengths.

The transitions 4f→3d and 4d→3p in O^{5+} can not be resolved in Fig. 12. However, the transition 4p→3s at about 450 Å should be resolved, but we do not observe an appreciable intensity for this line as opposed to that observed in Fig. 15. While it may be that the spectrometer efficiency is lower for 450 Å than for 520 Å, this may also be due to the slightly higher collision energy in our experiment which tends to populate the high angular momentum states more efficiently.

Searching for signatures of transfer-excitation, we also investigated the 78 keV O^{6+} + Ar collision system. Two spectra centered at 508 Å and 932 Å are shown in Fig. 16 and 17. The lines are identified in table 4. Again the spectra are dominated by O^{5+} lines.

We note however weak lines (E_1 - E_3) in Fig. 17. These lines are also listed in table 4. Similar lines were not observed for the O^{6+} + He collision system. Assuming the identification is valid, lines E_1 and E_2 are associated with transitions arising from Ar^{2+},

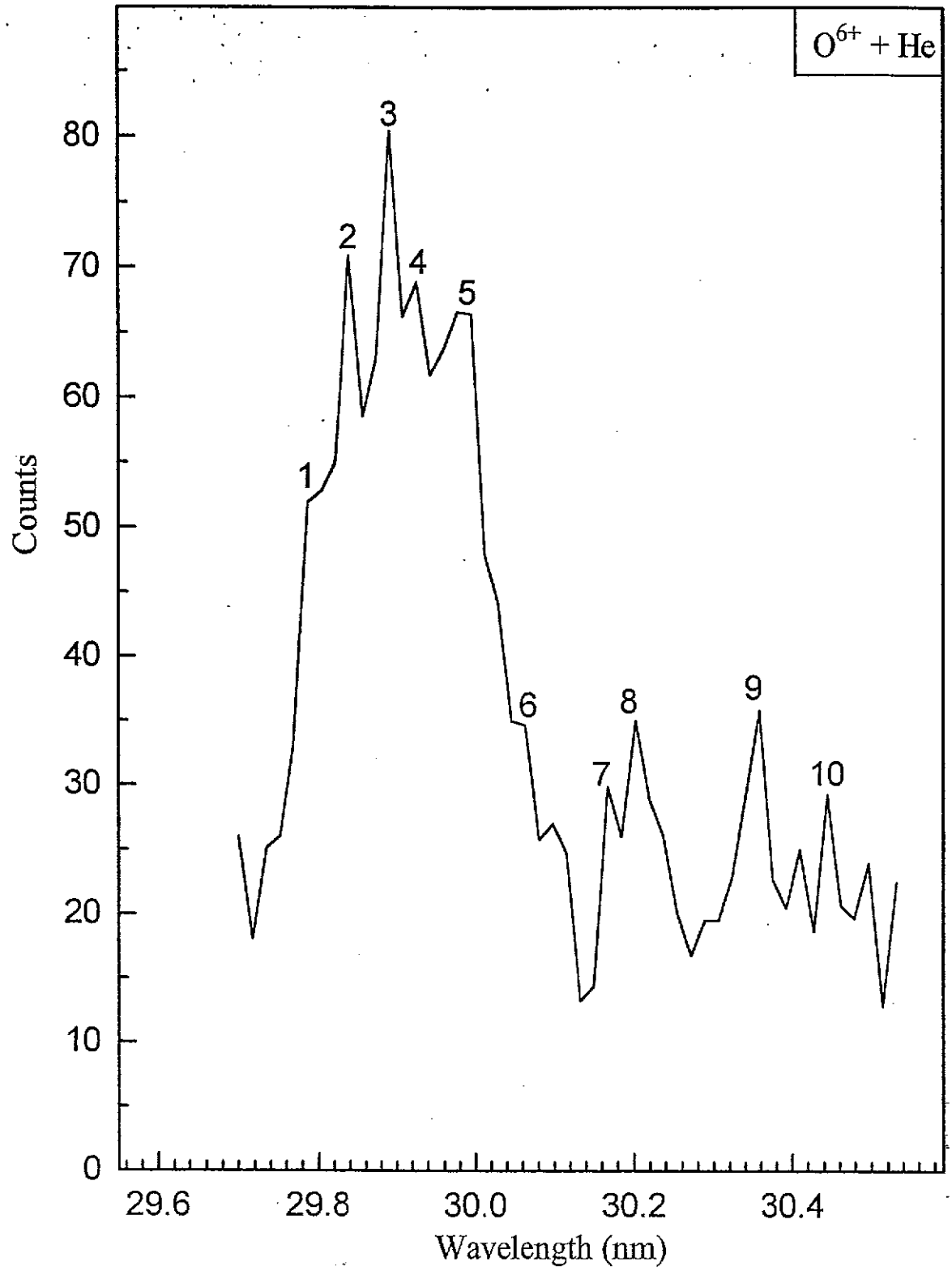

Fig. 14 : High resolution spectrum obtained for 60 keV O^{6+} + He collisions [34].

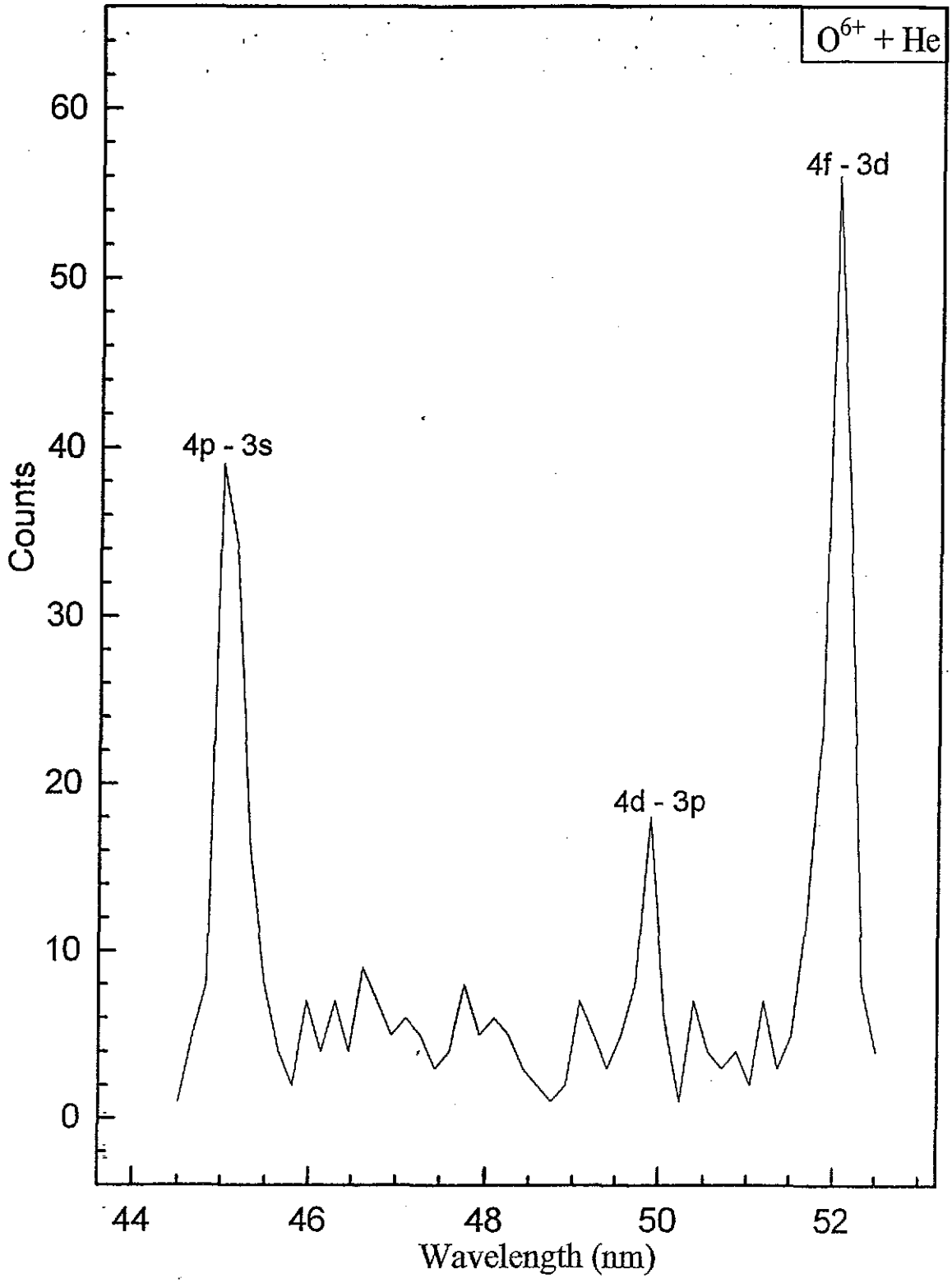

Fig. 15 : High resolution spectrum obtained for 60 keV O^{6+} + He collisions [34].

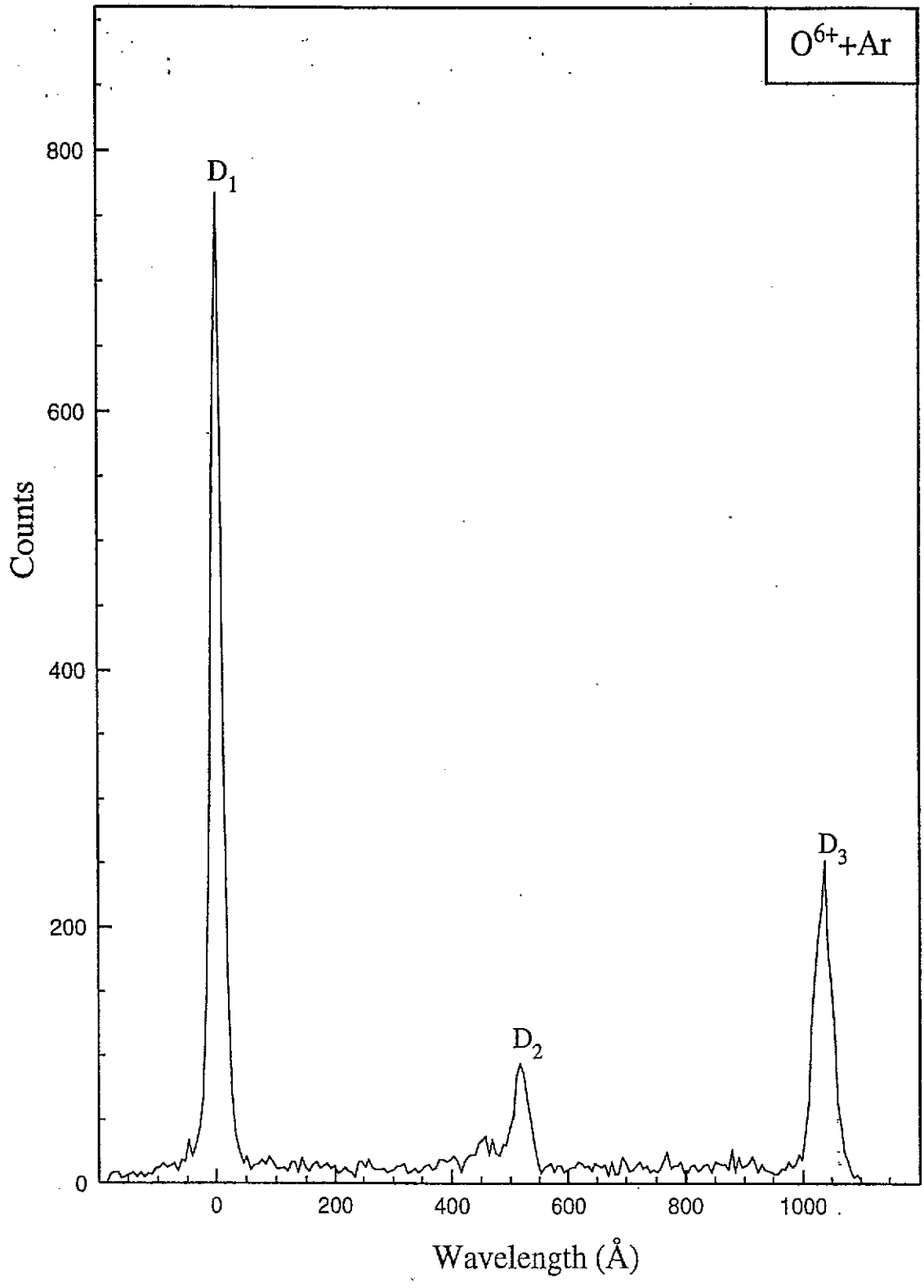

Fig. 16 : Spectrum obtained in O^{6+} + Ar collision. The spectrum is centered at 508 Å. See table 4 for identification of the prominent lines.

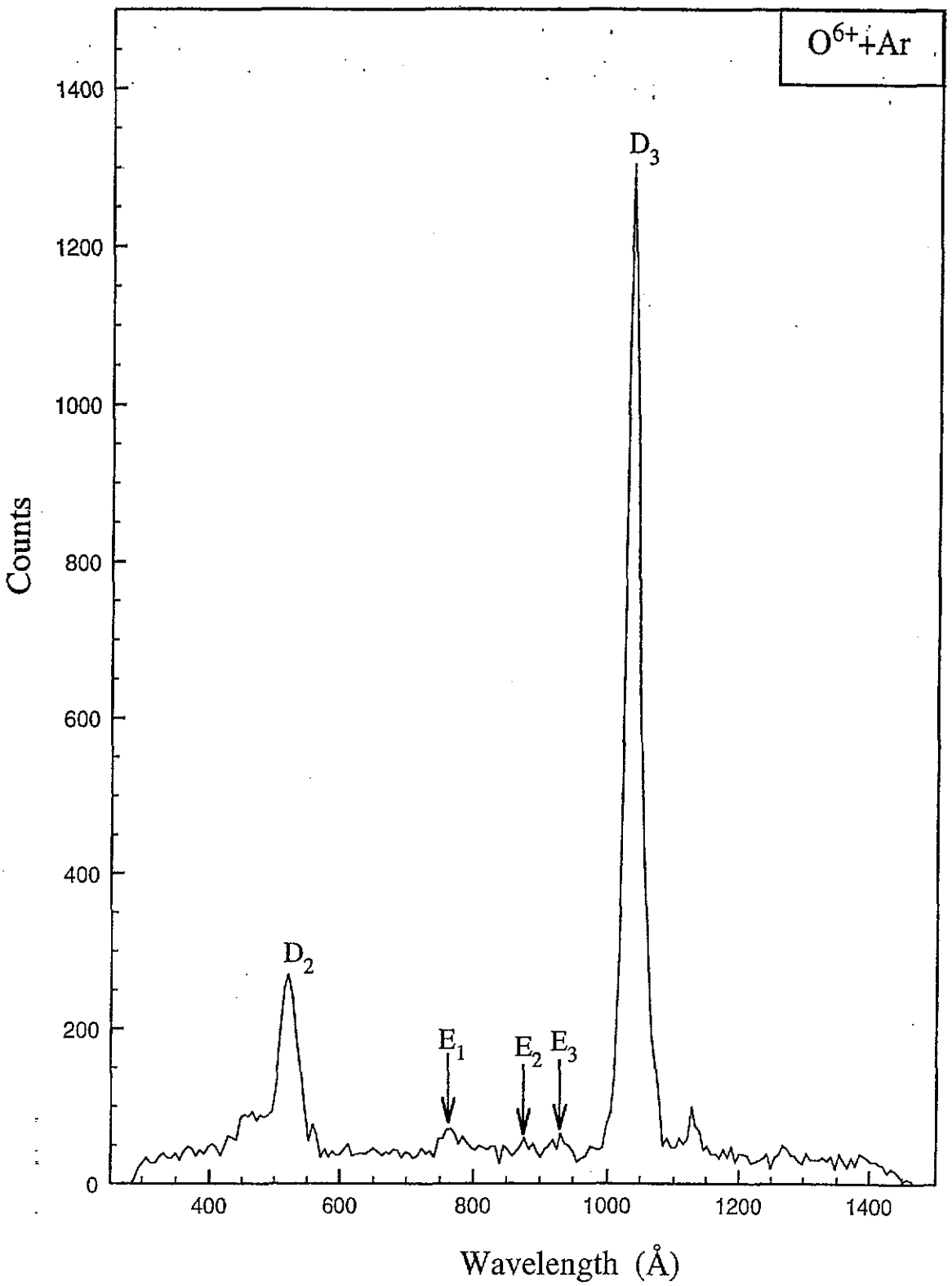

Fig. 17 : Spectrum obtained in O^{6+} + Ar collision. The spectrum is centered at 932 Å. See table 4 for identification of the prominent lines

Table 4 : Experimental wavelengths observed in O^{6+} + Ar collisions (figures 16 and 17) Line identification is obtained from the tabulation by Kelly [29]. The associated transitions and the radiating species are also given.

Label	Wavelengths (Å)	Transition Initial state-Final state	Radiating Species
D_1	Zero-order		
D_2	519.6	$1s^2 4f\ {}^2F_{5/2} - 1s^2 3d\ {}^2D_{3/2}$	O^{5+}
	519.7	$1s^2 4f\ {}^2F_{5/2} - 1s^2 3d\ {}^2D_{7/2}$	O^{5+}
	498.4	$1s^2\ 4d\ {}^2D_{5/2} - 1s^2 3p\ {}^2P_{3/2}$	O^{5+}
D_3	1031.9	$1s^2 2p\ {}^2P_{3/2} - 1s^2 2s\ g\ {}^2S_{1/2}$	O^{5+}
	1037.9	$1s^2 2p\ {}^2P_{1/2} - 1s^2 2s\ g\ {}^2S_{1/2}$	O^{5+}
E_1	≈770	$3s\ 3p^5\ {}^1P_1 - 3s^2 3p^4\ {}^1D_2$	Ar^{2+}
E_2	≈880	$3s\ 3p^5 - 3s^2 3p^4$	Ar^{2+}
E_3	≈919	$3s\ 3p^6\ {}^2S_{1/2} - 3s^2 3p^5\ g\ {}^2P_{3/2}$	Ar^+
	≈932	$3s\ 3p^6\ {}^2S_{1/2} - 3s^2 3p^5\ g\ {}^2P_{1/2}$	Ar^+

while E_3 arises from Ar^+ and may be first indications for atomic target excitation in our experiments.

The small peak to the right of D_3 could not be associated with any known oxygen or argon lines, not even in second order. From the previous discussion it is clear that more work is needed if transfer-excitation processes are to be identified reliably. In future work we intend to improve the detector resolution, enhance the photon collection efficiency, increase the ion beam current, carry out more systematic investigations and collect data for extended periods of time to obtain better statistics. In addition, procedures for background subtraction will be developed.

Chapter 5

Summary and Conclusion

The new beamline at the multicharged ion research facility at UNR has been successfully tested for ion beam transport where several ion beams have been guided to the collision chamber. The VUV-spectrometer was the first detection instrument to be used for investigating ion-atom collisions, and the data acquisition system has performed as expected.

The first experiments in search of target excitation in slow collisions of ions with multi-electron target have shown efficient molecular target excitation, while atomic target excitation proved elusive. However, possible indications have been found in O^{6+} + Ar collisions. A number of improvements on the experimental conditions will be made in an effort to systematically investigate this process.

References

[1] M. Barat and P. Roncin, J. Phys. B 25, 2205 (1992), and referances therein.

[2] R. Ali, V. Frohne, C. L. Cocke, M. Stockli, S. Cheng and M. L. A. Raphaelian, Phys. Rev. Lett. 69, 2491 (1992).

[3] J. Arianer and R. Geller, Ann. Rev. Nucl. Sci. 31, 19 (1981).

[4] X. Da "Multicharged Ion Beam Transport and Analysis System For ECR Ion Sources", Master Thesis , University of Nevada, Reno, (1995).

[5] R. Rejoub and R. A. Phaneuf, private comminication (1996).

[6] Model VM-502-V, Acton Research Corporation, Box 215, 525 Main Street, Acton, Massachusetts 01720.

[7] Roentdek GmbH, Im Vogelshaag 8, D- 65779 Kelkhem, Germany.

[8] Sparrow Corporation, P.O. Box 6102, Mississippi State, MS 39762.

[9] CATSA Preamplifier, Physikalische Nachweigerate, Zimmerner Strasse 9, 64409 Messel, Germany.

[10] TENNELEC, model TC241.

[11] Phillips Scientific, model 7164.

[12] Phillips Scientific, model 774.

[13] TENNELEC, model TC454.

[14] Phillips Scientific, model 794.

[15] Sparrow Corporation, model SCM-301.

[16] H. Merabet, Ph.D thesis, Universite de Caen, France (1996).

[17] H. Ryufuku, K. Sasaki, T. Watanabe, Phys. Rev. A 21, 745 (1980).

[18] A. Niehaus, J. Phys. B: At. Mol. Phys. 19, 2925 (1986).

[19] A. Ba'ra'ny, G. Astner, H. Cederquist, S. Huldt, P. Hvelplund, A. Johnson, H. Knudsen, L. Liljeby, and K. -G. Rensfelt, Nucl. Instrum. Methots Phys. Res. B 9, 397 (1985).

[20] L. D. Zener, Phys. Sovietunion 2, 46 (1932), C. Zener, Proc. Roy. Soc. A 137, 696 (1932).

[21] R. E. Olson and A. Salop, Phys. Rev. A 14, 579 (1976).

[22] H. Cederquist, Phys. Rev. A 43, 2306 (1991).

[23] H. Cederquist, E Beebe, C. Biedermann, A. Engstrom, H. Gao, R. Hutton, J. C. Levin, L. Liljeby, T. Quinteros, N. Selberg, and P. Sigray, J. Phys. B: At. Mol. Opt. Phys. 25, L69 (1992).

[24] P. Roncin, M. Barat, M. N. Goboriaud, L. Guillemot and H. Laurent, J. Phys. B 22, 509 (1989).

[25] W. Fritsch, J. Phys. B 27, 3461 (1994).

[26] H. O. Folkerts, F. Bliek and R. Hoekstra, , J. Phys. B 27, 3475 (1994).

[27] R. Bruch, V. Kantsyrev, V. Golovkina, A. Shlyaptseva, I. Golovkin, and R. Phaneuf, Rev. Sci. Instrum. 68, 1(1997), in press.

[28] W. Fritsch, Physics Letters. A 192, 369 (1994).

[29] R. L. Kelly " Atomic and Ionic Spectrum Lines Below 2000 Angstroms: Hydrogen Through Argon" Oak Ridge National Laboratory. october (1982).

[30] J. M. Ajello, G. K. James, B. O. Franklin and D. E. Shemansky, Phys. Rev. A 40, 3524 (1989).

[31] G. K. James, J. M. Ajello, B. O. Franklin and D. E. Shemansky, J. Phys. B : At. Mol. Opt. Phys. 23, 2055 (1990).

[32] D. Dijkkamp, D. Ciric, E. Vlieg, A. de Boer and F. J. de Heer, J. Phys. B 18, 4736 (1985).

[33] V. Kantsyrev, R. Bruch, M. Bailey, and A. Shlyaptseva, Appl. Phys Lett. 66, 3567 (1995).

[34] R. A. Phaneuf, R. Bruch, X. Da, V. Golovkina, I. Golovkin, V. Kantsyrev, H. Li, R..Rejoub, A. Shlyaptseva, J. K. Swenson, D. Hitz, V. V. Afrosimov and A. P. Shergin, Proceedings of the Fourteenth International Conferance on the Applications of Accelerators in Research and Industry, Denton, Texas (1996), in press; R. A. Phaneuf, V. Kantsyrev, V. Golovkina, A. Shlyaptseva, I. Golovkin and R. Bruch, presented at the Second Joint UNLV-UNR Nevada EPSCoR Chemical Physics Workshop, Tonopah, Nevada, October (1996).